MALAYSIAN JOURNAL OF ANALYTICAL SCIENCES

Journal homepage: https://mjas.analis.com.my/

Research Article

Synthesis and characterization of silver-loaded activated carbon for microfiber removal from laundry wastewater

Dahalan Sukor[1], Iwani W. Rushdi[1], Nur Sakinah Roslan[4], Maisarah Jaafar[1], Noorlin Mohamad[1], Yusof Shuaib Ibrahim[1,2], Wan Mohd Afiq Wan Mohd Khalik[1], Sabiqah Tuan Anuar[1], Sofiah Hamzah[3], Asmadi Ali@Mahmud[3], Nor Salmi Abdullah[4], Nasehir Khan E.M Yahya[4], Ahmad Fuad Shahruddin[5] and Alyza A. Azmi[1,3*]

[1]Microplastic Research Interest Group (MRIG), Faculty of Science and Marine Environment, Universiti Malaysia Terengganu, 21030 Kuala Nerus, Terengganu, Malaysia.
[2]Institute of Oceanography and Environment (INOS), Universiti Malaysia Terengganu, 21030 Kuala Nerus, Terengganu, Malaysia.
[3]Environmental Sustainable Materials Research Interest Group, Universiti Malaysia Terengganu, 21030 Kuala Nerus, Terengganu, Malaysia.
[4]Water Quality Laboratory, National Water Research Institute of Malaysia (NAHRIM), Lot 5377, Jalan Putra Permai, Rizab Melayu Sungai Kuyoh, 43300, Seri Kembangan, Selangor, Malaysia.
[5]Raf Technologies Sdn Bhd, 17, Jalan Meranti Jaya 8, Taman Perindustrian Meranti Jaya, 47120 Puchong, Selangor, Malaysia.

*Corresponding author: alyza.azzura@umt.edu.my

Received: 11 August 2025; Revised: 10 November 2025; Accepted: 10 December 2025; Published: 28 December 2025

Abstract
The discharge of microfibers (MFs) from domestic laundry effluents contributes significantly to microplastic pollution. In this paper, silver nanoparticle-loaded activated carbon (AC-Ag) was synthesized from rice husk through thermal–chemical activation followed by silver deposition. Material characterization using XRD, FTIR, XPS, SEM, and BET confirmed the formation of an amorphous carbon matrix with embedded face-centered cubic silver nanoparticles and a hierarchical porous structure favourable for MF capture. AC-Ag achieved 94-99% removal efficiency, surpassing bare rice husk activated carbon (~72-77%). MF removal was optimized using Response Surface Methodology (RSM) with a Box-Behnken Design (BBD) considering flow rate, MF loading, and AC-Ag bed height. Across 17 runs, AC-Ag achieved optimum MFs removal of 97.33% at 25.0 ml/min flow rate, 50 MFs, and 0.2 cm AC-Ag bed height. The quadratic model showed excellent predictive accuracy ($R^2 = 0.9865$, $p < 0.0001$), identifying adsorbent bed height as the dominant factor. Enhanced performance was attributed to increased residence time and multilevel pore trapping facilitated by the silver-modified porous carbon. These findings demonstrate that AC-Ag derived from agricultural waste are an effective and sustainable material for mitigating MF pollution in domestic wastewater.

Keywords: microplastic, nanoparticle, activated carbon, adsorbent, response surface methodology

Introduction

Microplastics (MPs), defined as synthetic polymers smaller than 5 mm, have emerged as a significant environmental concern, particularly in aquatic ecosystems. Among the various types of MPs, microfibers (MFs) shed from synthetic textiles during laundering are recognized as a major contributor of the MPs pollution in aquatic environments. It is estimated that global emissions of from domestic laundering of synthetic textiles amount to around 0.28 million tons annually, with 35% of the total MFs found in oceans originating from the laundering of synthetic clothing [1]. MFs are primarily composed of synthetic polymers such as polyester, nylon, and acrylic and are typically less than 10 µm in diameter. Several studies have reported the ubiquitous presence of MFs in both marine and freshwater environments, raising concerns about their persistence, bioaccumulation potential, and ability to transport harmful contaminants through the food chain [2,3]. Conventional wastewater treatment plants (WWTPs) are capable of removing up to 98–99% of MPs during primary treatment. However, a significant fraction of the MPs, particularly smaller MFs that fall below the filtration

capabilities of the treatment systems, still escape into the environment and are discharged into the aquatic ecosystem [4]. Therefore, there is an urgent need to develop and implement effective mitigation strategies within wastewater treatment plants to reduce the release of MFs into the environment.

In this study, we report the synthesis and characterization of a silver-loaded activated carbon (AC-Ag) composite derived from rice husk, designed as an effective adsorbent and filtration medium for removing MFs from laundry wastewater. While activated carbon (AC) is recognized for its excellent adsorption properties and has been widely used for various contaminants, and while silver nanoparticle (AgNP) integration has been documented for disinfection, a significant research gap remains. Specifically, there is a lack of studies on sustainable, waste-derived composites engineered for the specific physical entrapment of fibrous MPs under dynamic flow conditions. Furthermore, the operational parameters for such a system have not been systematically optimized. This work addresses these gaps by synthesizing a composite from agricultural waste (rice husk) functionalized with AgNPs to enhance MF entrapment through modified surface topography and interactions, and employing Response Surface Methodology (RSM) to systematically optimize the fixed-bed filtration process considering MF loading, contact time, and column height for maximum MF removal, thereby advancing toward practical, scalable wastewater treatment applications. The recyclability of the synthesized AC-Ag composite was also evaluated to assess its practical potential.

Materials and Methods

Materials

The rice husk used as raw material for activated carbon preparation was bought from a local company in Terengganu. The chemicals used in this experiment consist of ethanol, sodium hydroxide (NaOH), polyvinyl pyrrolidone (PVP), and silver nitrate salt ($AgNO_3$). All chemicals were analytical grade purchased from Sigma-Aldrich and used without prior purification. Deionized water was used for all the experiments.

Preparation of activated carbon (AC) from rice husk

Activated carbon was prepared following a method described in previous works [5-7] with slight modifications (**Figure 1**). The rice husk was oven-dried at 85 °C overnight and carbonized at 400 °C under nitrogen for 2 hours at a rising rate of 5 °C min^{-1}. Then, the carbonized rice husk was treated with NaOH and heated at 800 °C at 5 °C.min-1 for 1 hour. The resulting black powder was washed with deionized water until reaching a near-neutral pH, dried at 60 °C overnight, and ground.

Preparation of silver-loaded activated carbon (AC-Ag) composite

AgNPs were incorporated by dispersing 100 mg of rice husk carbon powder in 100 mL of water and sonicated for 30 minutes. Next, 3 g of PVP was dissolved in the suspension, and 20 mL of 1 mM $AgNO_3$ aqueous solution was rapidly added. The reaction proceeded at 65 °C with continuous stirring for 12 hours in a dark place to allow a stable and uniform formation of AgNPs. The product was collected via centrifugation, washed with deionized water several times, and dried under vacuum at 60 °C overnight.

Composite characterization

The structural and morphological characteristics of RHAC and AC-Ag composites were analyzed using Scanning electron microscopy (SEM) coupled with Energy Dispersive Spectroscopy (EDS) (Bruker, Xflash 600 Mini) and High Resolution-Transmission Electron Microscope (HR-TEM) (JEOL, JEM-ARM 200 F, Japan). The crystal structure was determined using X-ray diffraction (XRD) with Cu Kα radiation. X-ray Photoelectron Spectroscopy (XPS) analysis was conducted with an AXIS Ultra DLD (Kratos, UK) system equipped with an Al Kα X-ray source (1486.6 eV) at 8 mA emission and 15 kV anode high voltage. Fourier Transform Infrared (FTIR) spectra were recorded using a Bruker INVENIO spectrophotometer within the 4000 – 500 cm^{-1} range and analyzed using OPUS software. Pore size distribution and N_2 adsorption–desorption isotherms were assessed using an aperture analyzer (Quantachrome, USA), with specific surface area calculations performed using the BET method.

Quantification and characterization of MFs particles

Domestic laundry wastewater samples (500 mL) were filtered using 47 mm Whatman GF/F filter papers (1.2 µm pore size). Sample bottles were rinsed three times with filtered ultrapure water during filtration to minimize MF particle loss. The filter papers were then transferred to glass petri dishes, covered with aluminum foil to prevent airborne contamination, and dried in a desiccator for 24 hours. MFs were identified under a stereomicroscope model SZ 51 from OLYMPUS (Japan) with magnification at 0.8–4.0X and equipped with a Dino-Eye Eyepiece Camera in a designated chamber for MF sorting. The surface morphology of the collected MFs was examined using Scanning electron microscopy (SEM) (Bruker, Xflash 600 Mini), and the molecular vibrations of the polymer molecules were confirmed using Fourier Transform Infrared (FTIR) spectrophotometer (Bruker, INVENIO S)

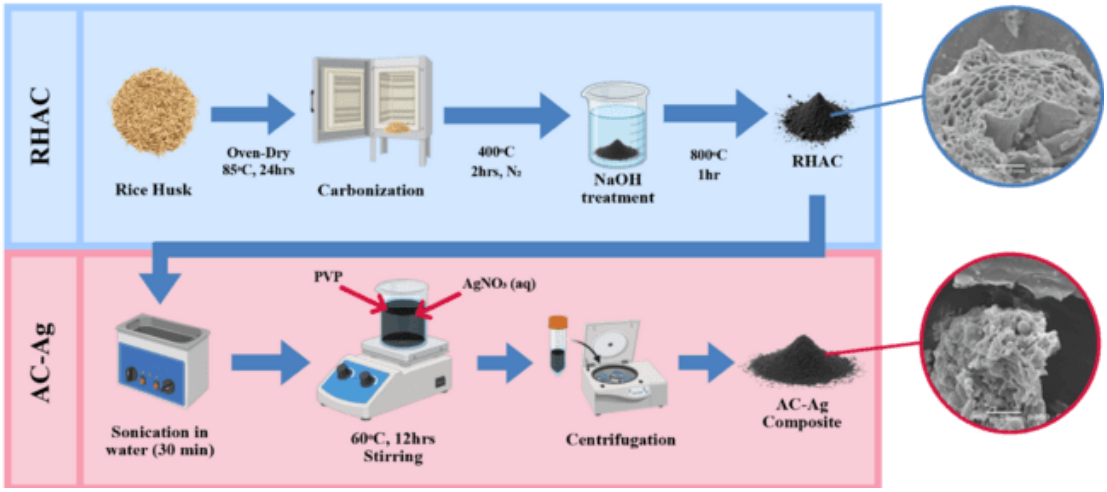

Figure 1. Schematic of the preparation of AC-Ag

Contamination control

To minimize MPs contamination, a strict protocol was followed. All glassware and pipettes were soaked in methanol for 24 hours and rinsed thrice with ultra-pure deionized water. A blank control experiment were performed before each batch of sample analysis and intermittently during experimental runs to eliminate contributions from plastic products, and plastic equipment was avoided. Pre-rinsing steps were implemented, and personal protective measures, such as nitrile gloves and 100% cotton lab coats, were employed.

MFs removal efficiency

The MF particle removal study was conducted using a fixed-bed column filtration system experiment. The AC-Ag composite was packed into the middle section of a glass filtration column (length = 7 cm, diameter = 15 mm). the packing of the filter media was accomplished through an elution method, where deionised water was passed through the column to remove air voids. This process was repeated until the desired bed height was achieved. A thin layer of wool was placed between the AC-Ag bed to prevent the sudden movement of AC-Ag composite into the effluent stream. The water sample containing a certain amount of MFs (was introduced and passed through the column at a flow rate of 70 mL/min under gravitational assistance and facilitated by a peristaltic pump. Each experiment was conducted three times, and the average removal rate was calculated. The resulting filter paper was examined under a dissecting microscope to identify any MFs that had passed through the adsorbent during the fixed-bed column test. The test was then repeated with RHAC to compare the filter's efficiency.

The removal rate of MFs was calculated using the following formula:

$$\text{The removal rate of MFs} = \frac{x-y}{x} \times 100\% \qquad (1)$$

where x is the initial amount of MFs before passing through the column and y is the removal of MFs after passing through the column.

Box-Behnken design (BBD)

Experimental conditions for MFs removal from laundry wastewater using AC-Ag composites were optimized via BBD. The effects of three factors (MFs loading, bed height, and flow rate) at three levels (low, medium, and high, coded as −1, 0, and +1) were investigated (Table 1). Triplicate experiments were performed, and results were analyzed using ANOVA to estimate second-order regression coefficients. A second-order polynomial equation was plotted to determine the optimal point precisely. Statistical analyses, including multivariable equations and regression modeling, were performed using Design Expert software (Version 13, State-Ease, USA).

Table 1. Values of experimental design variables

Factor	Variables	Levels of Variables		
		−1	**0**	**+1**
A	Loading of MFs	50	525	1000
B	Bed height (cm)	0.1	0.2	0.3
C	Flow rate (ml min-1)	25.0	70.0	47.5

Results and Discussion

Characterization of MFs

To confirm the chemical identity of the extracted MFs from laundry wastewater, Fourier-Transform Infrared Spectroscopy (FTIR) analysis was conducted, and the spectra were compared against reference profiles for common synthetic polymers. **Figure 2** displays the overlaid FTIR spectra for the isolated fibers and their respective polymer standards. The FTIR spectrum of the sample identified as polyamide (PA) closely resembles that of the PA reference, exhibiting distinct absorption bands characteristic of polyamide structures. Notable peaks include the broad N–H stretching vibration at approximately 3299 cm^{-1} and the C–H stretching around 2930 cm^{-1}. A strong amide band is observed at 1634 cm^{-1}, corresponding to C=O stretching vibrations, while the second amide band appears at approximately 1541 cm^{-1} and 1462 cm^{-1} due to N–H bending and C–N stretching modes. The sharp absorption at approximately 1370 cm^{-1} is attributed to CH_2 wagging vibrations, and the band near 1200 cm^{-1} signifies C–N stretching. These peaks collectively confirm the presence of nylon 6 based polyamide, supporting the identification of the sample as a synthetic fiber derived from PA [8].

Similarly, the FTIR spectrum (**Figure 3**) of the second MF sample demonstrates a strong correlation with the polyethylene terephthalate (PET) reference. Distinct absorption bands were recorded around 1714 cm^{-1}, corresponding to C=O stretching of ester linkages in PET. Peaks at 1238 cm^{-1} and 1093 cm^{-1} represent asymmetric and symmetric C–O stretching vibrations, respectively, while the band at approximately 1550 and 1450 cm^{-1} is associated with ring vibrations of the aromatic benzene unit. Moreover, a peak near 722 cm^{-1} signifies the presence of out-of-plane C–H bending of the aromatic ring. The presence of these characteristic PET signatures indicates that the isolated fibers contain PET, consistent with common textile-originated MFs [9]. The close spectral overlap between the environmental samples and their respective reference standards indicates minimal chemical degradation or oxidation of the MFs during laundering or environmental exposure. This suggests that the released MFs retain their native polymeric structure, which can influence their environmental persistence and interaction with adsorbent materials like AC-Ags. The clear match between characteristic absorption bands supports confident identification of the fibers as PA and PET. The predominant detection of PA and PET fibers is reasonable and reflects regional textile consumption patterns, where polyester and nylon dominate the synthetic apparel market [10,11].

To investigate the surface morphology of the extracted MFs, SEM analysis was conducted at 1000× and 2000× (**Figure 4**). The MFs exhibit elongated cylindrical structures typical of synthetic fibers. On closer inspection, various degradation markers such as longitudinal cracks, delamination grooves, and particle adhesion are evident. **Figure 4a** shows a MF with a partially detached outer layer and visible ridges, indicating structural fatigue and fiber fibrillation which is a phenomenon commonly associated with repeated washing cycles. The attached loop-like strand may result from entanglement or shedding during laundry agitation [12].

In contrast, **Figure 4b** highlights a MF exhibiting severe surface disruption, including pitting, tearing, and the presence of fragmented residues attached to its surface. These adhering substances may represent particulate matter, detergent residues, or fragmented fibers, potentially originating from other garments during washing. This type of adhesion, particularly of film-like material and fibrous debris, aligns with previous observations of particle agglomeration due to ambient exposure or surfactant-driven interactions in laundering environments [13]. Additionally, the presence of cracks along the fiber axis suggests photooxidative degradation and hydrolytic stress, consistent with the prolonged aging and repeated mechanical abrasion of textiles. The cracking patterns may reflect cyclic stress and strain imparted during washing, drying, and usage, which ultimately contribute to fiber detachment from the fabric matrix [12,14].

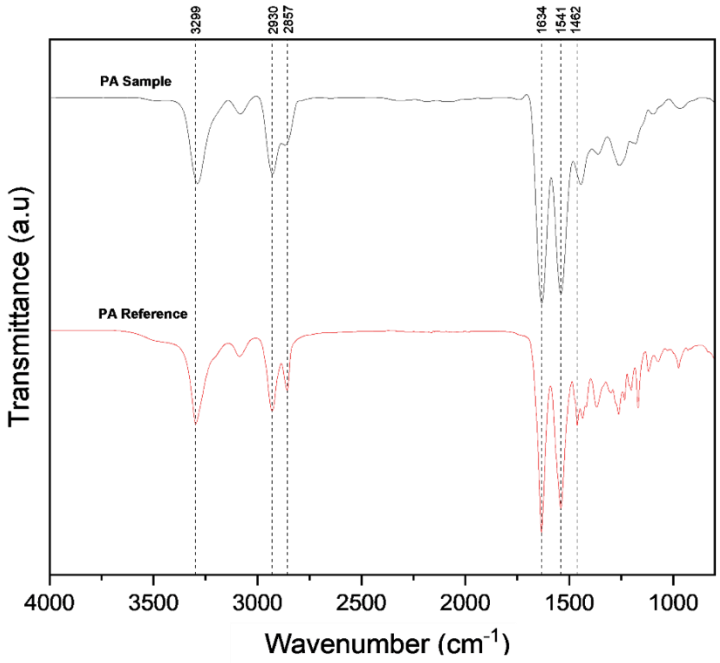

Figure 2. FTIR of PA sample against the reference spectrum

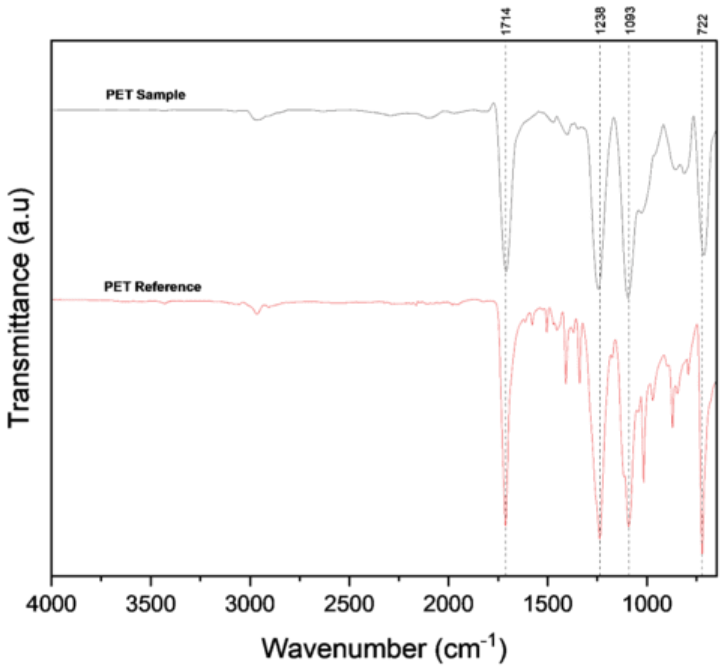

Figure 3. FTIR of PET sample against the reference spectrum

a. b.

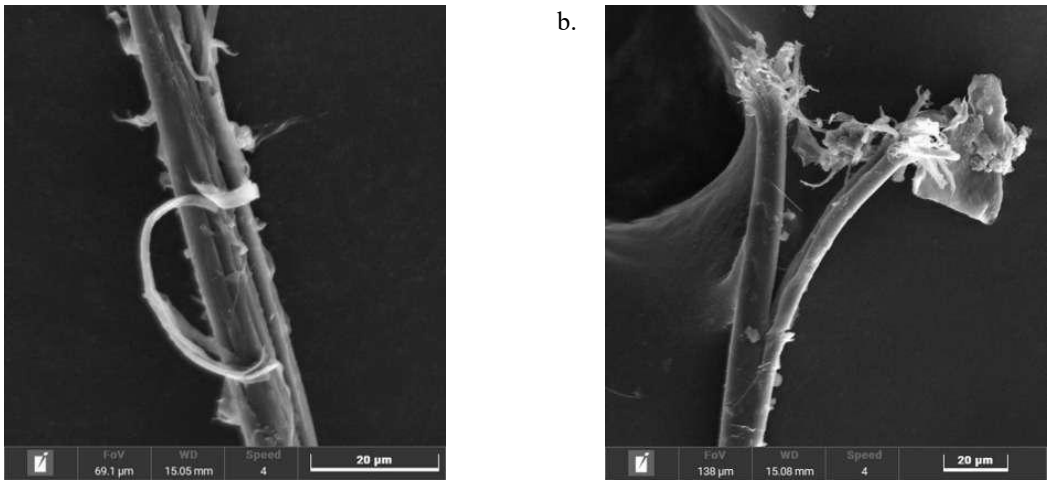

Figure 4. SEM images at 1000× magnification (a) and 2000× magnification (b) of MF samples

Physico-chemical characterization of the RHAC and AC-Ag composites

The SEM images presented in Figure 5 illustrate the structural characteristics of RHAC and AC-Ag composite at varying magnifications. The RHAC exhibits a honeycomb-like morphology with surface holes, a result of chemical activation using NaOH (**Figure 5a**) [15]. This activation process enhances the porosity of the carbon structure and facilitates the development of a network of interconnected pores [16]. The incorporation of AgNPs into the AC significantly increases surface roughness, as evidenced by their presence on the surface and within interstitial spaces between AC particles (**Figure 5b**). This modification leads to a reduction in the visibility of pores and cavities, indicating successful loading of AgNPs into the AC framework [17]. TEM analysis (**Figure 5c**) confirmed the presence of spherical dark dots corresponding to AgNPs, with an average size of approximately 4 – 6 nm, smaller than the pore size of the AC. The EDS pattern (**Figure 5d**) further elucidates the chemical composition of the AC-Ag composite. The EDS pattern reveals distinct peaks for carbon (C), silver (Ag), and silicon (Si), confirming the successful incorporation of AgNPs into the AC matrix. In addition, the C and Si peaks are attributed to the rice husk-derived AC.

The XRD patterns of the synthesized RHAC and AC-Ag are presented in **Figure 6**. displays a broad diffraction band within the 2θ range of 15–30°, indicative of the amorphous nature of activated carbon [6]. This amorphous structure likely arises from the disordered arrangement of carbon atoms following thermal and chemical activation of the rice husk precursor [18,19]. The RHAC lacks any well-defined peak indicating a predominantly amorphous structure. Meanwhile for AC-Ag, in addition to the amorphous peak, sharp peaks at 2θ values of 21.8° and 42.5°, which are indexed to the (002) and (100) planes of graphitic carbon are observed (JCPDS no. 75-1621). These features indicate that a fraction of the carbon in the composite may exhibit localized graphitic ordering, likely due to structural rearrangement during incorporation of silver.

Additionally, multiple Bragg reflections at 2θ = 28.3°, 31.3°, 38.0°, 44.1°, 46.9°, 54.1°, 57.0°, 64.3°, and 77.2° were recorded, corresponding to the (210), (122), (111), (200), (231), (142), (241), (220), and (311) planes of elemental silver (JCPDS No: 04-0783) [20]. These peaks confirm the high phase purity and crystalline integrity of the silver nanoparticles and are a characteristic reflection of face-centered cubic (FCC) structured AgNPs [17,21]. The calculated phase distribution for AC-Ag reveals that the sample comprises 32.03% crystalline and 67.97% amorphous components. The crystalline fraction is predominantly attributed to silver and the graphitic carbon, while the amorphous contribution stems from the activated carbon framework. The coexistence of carbon- and silver-related diffraction peaks within the same XRD pattern demonstrates that the silver nanoparticles remained structurally stable and well-integrated onto the AC support during synthesis [22].

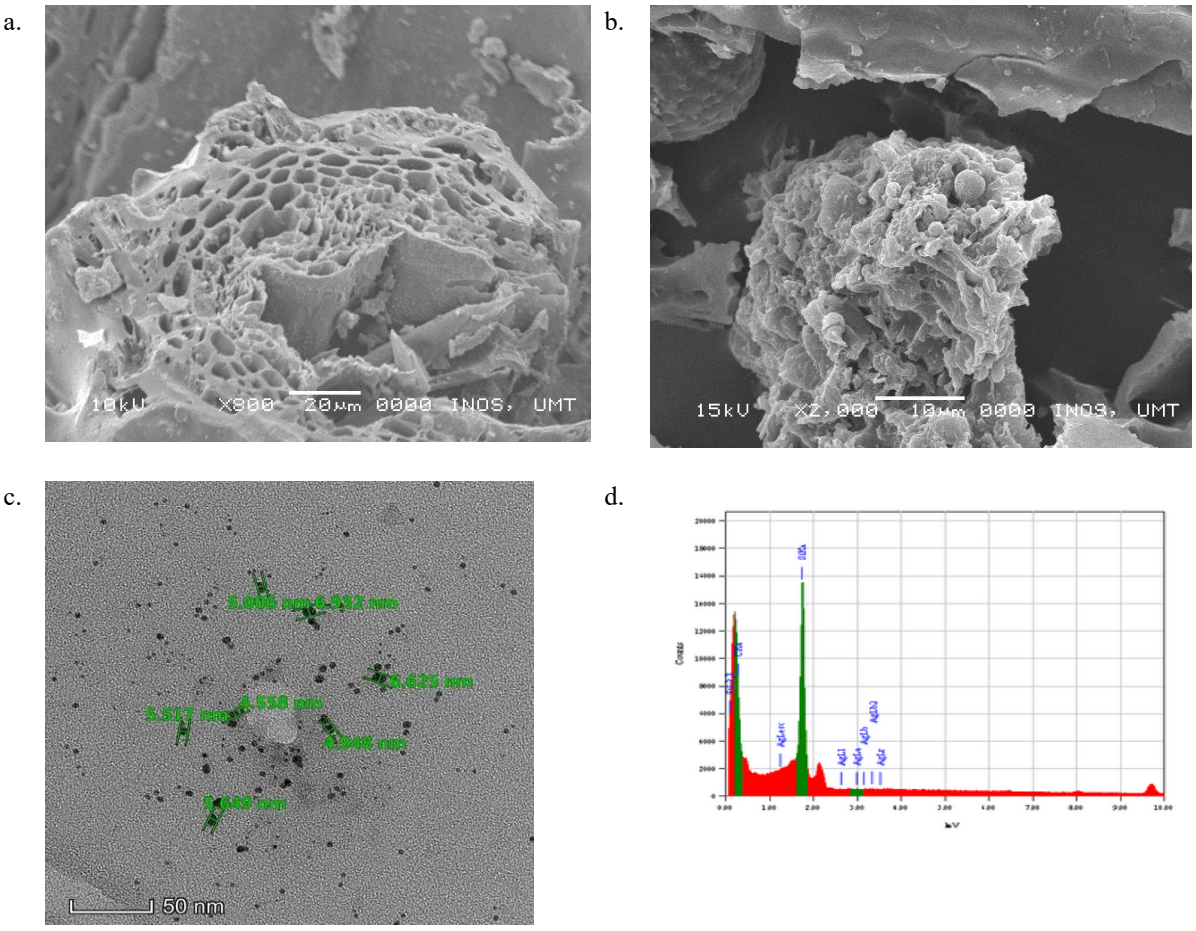

Figure 5. SEM images of RHAC (a), AC-Ag composite (b), TEM image (c) and EDS spectrum (d) of AC-Ag composite

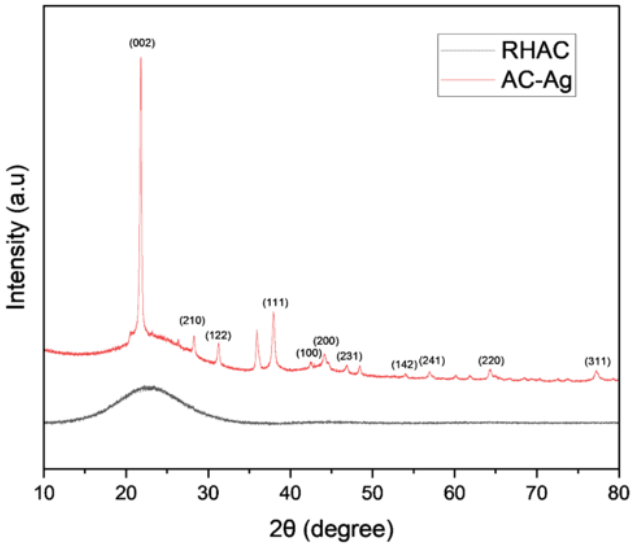

Figure 6. XRD pattern for RHAC and AC-Ag

To investigate the surface elemental composition and chemical states of the synthesized AC-Ag, X-ray photoelectron spectroscopy (XPS) was performed. The wide-scan spectrum in **Figure 7** reveals dominant peaks corresponding to carbon (C 1s) and silver (Ag 3d), confirming the presence of these key elements in the sample without noticeable impurities, indicating a clean synthesis process [5]. The high-resolution C 1s spectrum displays a prominent peak at approximately 284 eV, which is characteristic of carbon-based functional groups typically found in activated carbon. This peak is attributed to the C–C/C=C bonds of sp^2 hybridized carbon atoms and minor contributions from oxygen-containing groups like C–O or O–C=O [23]. These functionalities enhance the surface reactivity and aid in the immobilization of silver nanoparticles [17]. The Ag 3d spectrum shows two well-resolved peaks in the range of 367–375 eV, which correspond to Ag $3d_{5/2}$ and Ag $3d_{3/2}$ spin-orbit components. The energy separation between these peaks, approximately 6 eV, is consistent with the characteristic signature of metallic silver (Ag^0), confirming the reduction of silver ions during the synthesis process [24]. These findings indicate that the majority of silver exists in the elemental (metallic) state, strongly suggesting successful incorporation of AgNPs onto the activated carbon matrix. This supports the effective and stable loading of silver nanoparticles on the AC surface, which is crucial for their application in MF removal from wastewater.

The FTIR spectra of raw rice husk, RHAC and AC-Ag are illustrated in **Figure 8**. For the raw rice husk, a broad absorption band centered around 3536 cm^{-1} is observed, which corresponds to the O–H stretching vibration of hydroxyl groups [25]. Notable peaks at 2922 cm^{-1} and 2350 cm^{-1} are assigned to C–H stretching and C=O (CO_2) stretching vibrations, respectively [26]. The absorption around 1750 cm^{-1} corresponds to carbonyl stretching (C=O), indicative of ketones, aldehydes, or carboxylic groups. Bands within 1300–900 cm^{-1} are associated with C–O stretching in esters, ethers, and phenolic compounds, while peaks around 1187 cm^{-1} indicate C–N stretching. Cellulose presence can be observed by the appearance of C-OH bending at a wavenumber of 1095 cm^{-1} [27]. The band at 588.86 cm^{-1} is due to Si-O-Si vibration [28].

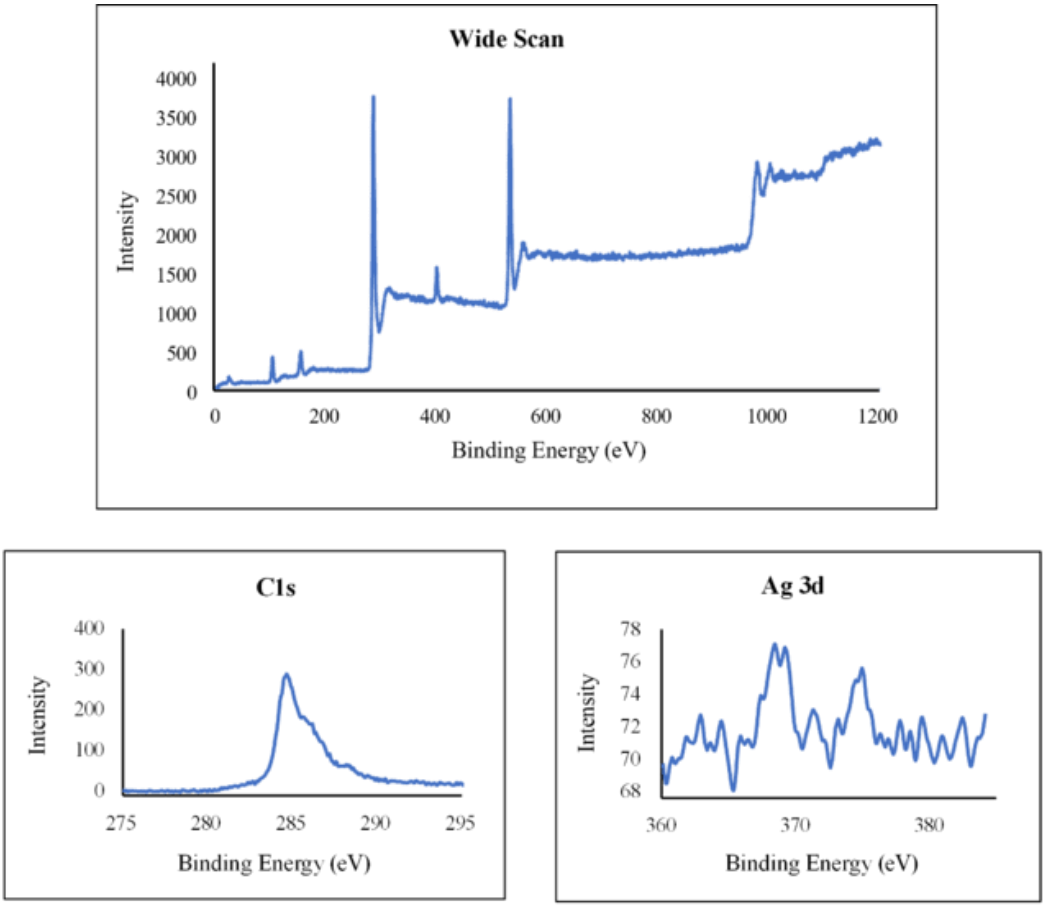

Figure 7. XPS spectra of the wide scan, C1s, and Ag 3d for the prepared AC-Ag

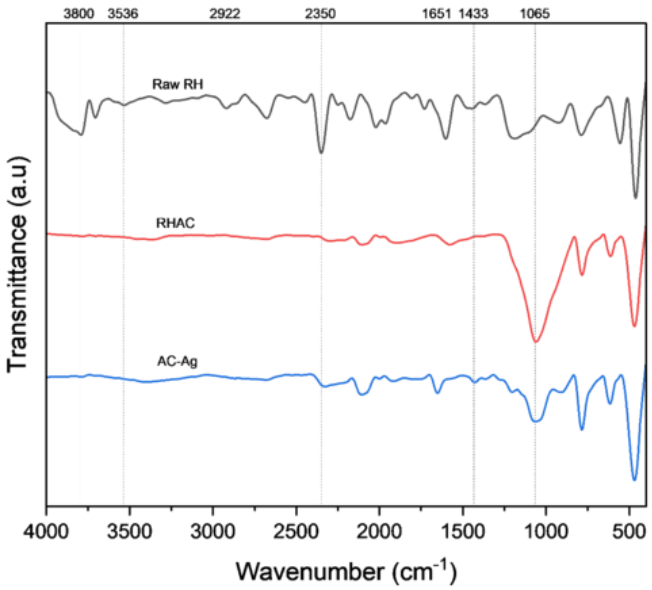

Figure 8. FTIR for raw RH, RHAC and AC-Ag

Following carbonization and activation, the FTIR spectrum of AC-Ag shows fewer absorption bands compared to raw rice husk, suggesting that some functional groups were thermally decomposed and released as volatile byproducts during high-temperature treatment [29]. Two peaks for C=C stretching in aromatic structures were found at 1569 cm^{-1} and 1446 cm^{-1} for RHAC while 1651 cm^{-1} and 1433 cm^{-1} for AC-Ag which is a characteristic of the carbon backbone in AC [28]. The absence of any new peaks also implies that no covalent bonds were formed between AgNPs and AC, and the interaction is likely due to coordination or surface adsorption [5].

Nitrogen adsorption–desorption isotherms were conducted at 77 K to evaluate the surface area and porosity of the prepared RHAC and AC-Ag (**Figure 9**). The isotherms exhibit features characteristic of Type IV curves, indicating that mesopores dominate the structure of both materials [30]. The BET surface area analysis reveals differing trends depending on the material. For RHAC and AC-Ag, the surface area of RHAC increases from 308.3 m^2/g to 371.1 m^2/g upon Ag loading, along with an increase in pore volume from 0.226 to 0.296 cm^3/g. This enhancement may be attributed to improved textural properties or partial restructuring of the porous framework during nanoparticle integration [31].

MFs removal efficiency

The efficacy of RHAC and AC-Ag in removing MFs from water was assessed using a column filtration setup. The removal efficiency was tested under varying MF feed concentrations, ranging from 40 to 1000 pieces. **Table 2** summarize the performance comparison between RHAC and AC-Ag and shows a clear divergence between the two materials. The removal rate of RHAC fluctuated between approximately 64.15% and 77.60% as MF feed increased, while AC-Ag consistently maintained removal efficiencies above 94%, peaking at 99.07%. The results indicate that AC-Ag consistently outperformed bare RHAC across all feed concentrations. At the lowest MF loading of 40 pieces, RHAC achieved a removal rate of 72.50%, whereas AC-Ag demonstrated a significantly higher removal efficiency of 94.17%. This trend remained consistent with increasing MF loads. For instance, at 200 MFs, bare RHAC showed a fluctuating removal rate where it dips to 68.00%, while AC-Ag maintained a stable and elevated efficiency of 97.50%.

As the MF feed increased from 400 to 1000 pieces, the removal performance of RHAC remained relatively inconsistent, ranging from 74.30% to 77.60%, suggesting limitations in adsorption capacity and retention efficiency. In contrast, AC-Ag retained a high removal percentage between 97.42% and 99.07%, even at the highest tested MF concentration of 1000 pieces. The consistently high performance of AC-Ag implies that the presence of silver nanoparticles enhanced MF entrapment by reinforcing the porous structure of the carbon matrix and possibly introducing additional binding interactions [32].

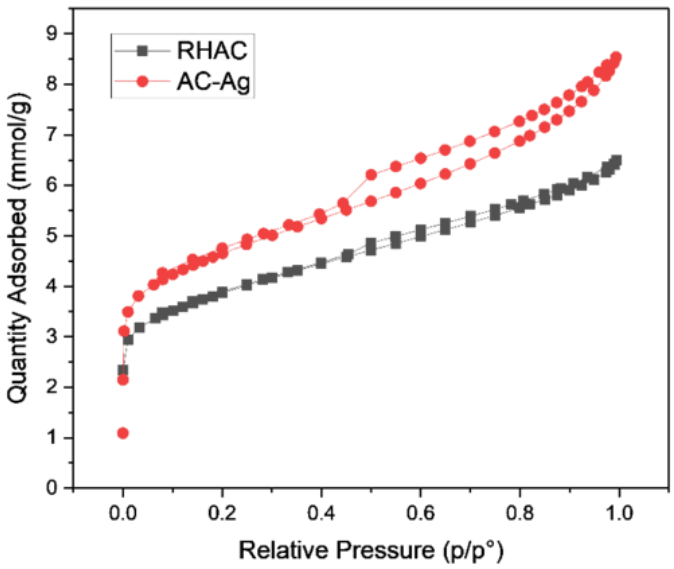

Figure 9. N_2 adsorption/desorption isotherm for RHAC and AC-Ag

The enhancement in removal efficiency can be attributed to several structural and chemical features of the AC-Ag. The base activated carbon, derived from rice husk, exhibited an amorphous porous structure formed during carbonization and activation, which served as physical traps for the MFs [33]. However, the inclusion of silver nanoparticles further improved this performance. The incorporation of AgNPs, likely stabilized within the pores through van der Waals forces and electrostatic interactions, further optimized the pore structure and introduced additional active sites [34]. The small amount of $AgNO_3$ used in the synthesis (0.1 M) suggests that the distribution of nanoparticles was confined within the pores, ensuring S_{bet} and pore volume remains high ensuring enhance selective entrapment mechanisms [35]. Due to the mismatch between the MF dimensions and the narrow pore openings of AC-Ag, a size exclusion effect likely contributed to the high removal rates [36]. Furthermore, the data aligns well with previous reports by Wang et al., which demonstrated that modified carbon-based filters achieved MPs removal rates exceeding 95%, with negligible release (<0.5%) upon backflushing. However, the focus was mainly on spherical MPs. While the shape of MPs can influence removal behavior, the high consistency of AC-Ag across a wide feeding range indicates strong adaptability to fiber-type MPs, which are more difficult to trap than spherical forms [37]. This mechanism is not exclusive to MFs. Hence, the AC-Ag composite should be effective for other MP shapes via size-exclusion and adsorption, so the high efficiency demonstrated here suggests broad applicability.

Table 2. Performance Comparison of RHAC and AC-Ag

Amount of MFs Feeding	RHAC	AC-Ag
40	72.50	94.17
80	72.63	98.33
120	76.08	96.39
160	73.93	95.83
200	68.00	97.50
400	77.60	97.42
600	75.05	99.05
800	77.08	98.67
1000	74.30	99.07

Optimization of MF Removal by RSM-BBD

The response surface optimization for MF removal using AC-Ag was designed through a 3-factor, 2-level BBD, comprising 17 experimental runs. The independent variables included flow rate (A: 25–70 mL/min), MF loading (B: 50–1000 units), and amount of AC-Ags (C: 0.1–0.3 cm). Analysis of variance (ANOVA) indicated that the quadratic model was statistically significant for predicting MF removal, with a model F-value of 56.86 and $p < 0.0001$, confirming that the model fit is not due to random variation (**Table 3**). The high R^2 value of 0.9685, along with an adjusted R^2 of 0.9692 and a predicted R^2 of 0.8421, further validated the reliability and predictive strength of the model [38]. The coefficient of variation (CV) was only 2.82%, suggesting good precision and reproducibility of the experimental system. Among the three main factors, the amount of AC-Ag (C) was the most influential ($F = 280.22$, $p < 0.0001$), followed by flow rate (A) and MF loading (B). Significant interaction effects were also found for AB, AC, and BC, indicating that the combined effects of these factors notably influenced the overall removal efficiency.

Table 4 presents the results of the 17 experimental runs. The actual removal efficiencies ranged from 54.33% to 97.33%, with the lowest performance observed at high flow rate and low AC-Ag loading (Run 9), and the highest efficiency recorded at low flow rate and low MF loading (Run 4). These trends are visualized in the response surface plots (**Figure 10**). In the response surface plot for flow rate vs. MF loading (**Figure 10a**), as the flow rate increased from 25 to 70 mL/min, the MF removal efficiency decreased, particularly under high loading conditions (1000 MFs). This is attributed to reduced residence time within the packed column. At high flow rates, the water passes through the AC-Ag bed more quickly, offering less contact time for mechanical entrapment or surface interaction between MFs and the adsorbent [39]. Simultaneously, high MF loading introduces a greater contaminant burden, which overwhelms the available binding and trapping sites. The combined effect leads to incomplete retention, especially at higher throughput rates, which has been commonly observed in fixed-bed filtration systems due to early saturation or "channelling" effects within the bed [40].

Meanwhile, for the response surface plot of flow rate vs. AC-Ag amount (**Figure 10b**), at any given flow rate for increasing the column height (0.1 to 0.3 cm of AC-Ag) significantly improved removal performance. This outcome is justified by the increased bed depth, which not only increases the total surface area available for interaction but also provides a longer filtration pathway, allowing more opportunities for MF entrapment through mechanical sieving, inertial interception, and adsorptive adhesion [41]. At lower flow rates, this effect is further amplified because MFs have more time to interact with the silver-decorated porous matrix, which may also offer electrostatic interactions or weak van der Waals attractions to synthetic fibers, depending on their polymer type and charge properties [41].

Table 3. ANOVA table for removal of MFs

Source	Sum of Squares	df	Mean Square	F-value	p-value	
Model	2660.50	9	295.61	56.86	< 0.0001	Significant
A	252.56	1	252.56	48.58	0.0002	
B	238.38	1	238.38	45.85	0.0003	
C	1456.92	1	1456.92	280.22	< 0.0001	
AB	110.36	1	110.36	21.23	0.0025	
AC	47.61	1	47.61	9.16	0.0192	
BC	36.00	1	36.00	6.92	0.0338	
A^2	88.00	1	88.00	16.93	0.0045	
B^2	391.83	1	391.83	75.36	< 0.0001	
C^2	34.10	1	34.10	6.56	0.0375	
Fit Statistic						
R^2	0.9685					
Adjusted R^2	0.9692					
Predicted R^2	0.8421					
C.V (%)	2.82					

**A: Flow rate (ml/min); B: Loading of MFs; C: Amount of AC-Ag (cm)*

Table 4. Design of experiment and results of the response surface design of removal of MFs

Run	A (ml/min)	B (-)	C (cm)	MFs Removal (%)	
				Predicted	Actual
1	25.0	1000	0.2	95.00	95.00
2	70.0	1000	0.2	73.25	71.33
3	47.5	1000	0.1	60.21	62.33
4	25.0	50	0.2	95.41	97.33
5	47.5	525	0.2	75.36	76.00
6	47.5	525	0.2	75.36	74.22
7	70.0	50	0.2	94.66	94.67
8	25.0	525	0.3	92.75	92.95
9	70.0	525	0.1	54.53	54.33
10	47.5	50	0.1	77.13	77.33
11	47.5	50	0.3	98.12	96.00
12	47.5	525	0.2	75.36	73.65
13	70.0	525	0.3	88.41	90.54
14	47.5	525	0.2	75.36	75.11
15	25.0	525	0.1	72.66	70.54
16	47.5	1000	0.3	75.36	93.00
17	47.5	525	0.2	75.36	77.84

**A: Flow rate (ml/min); B: Loading of MFs; C: Amount of AC-Ag (cm)*

At constant flow rate, increasing the amount of AC-Ag results in better removal performance, even at higher MF concentrations (Fig. 10c). Thicker adsorbe nt beds prevent premature channelling and provide m ultiple physical barrier layers, which can sequentially trap fibers that escape initial capture. When MF loadi ng increased, the removal performance remained relat ively stable as long as the AC-Ag column thickness w as sufficient (≥0.2 cm). This suggests that the system had enough adsorption/trapping capacity to handle in creasing MF loads, provided that the bed was not too thin. At lower AC-Ag thicknesses, particularly 0.1 c m, removal efficiency dropped sharply at high MF fe edings. This reinforces the importance of adsorbent q uantity in maintaining system resilience against break through events.

The second-order polynomial equation generated to model MF removal efficiency (Y) is:

$$Y = 75.364 - 5.61875A - 5.45875B + 13.495C - 5.2525AB + 3.45AC + 3BC + 4.57175A^2 + 9.64675B^2 - 2.84575C^2 \quad (2)$$

Perturbation plots (**Figure 11**) confirm that the AC-Ag amount (C) had the most pronounced positive effect on MF removal. In contrast, increased flow rate (A) and loading (B) generally had a negative effect, consistent with the surface response plots.

The optimal operating condition predicted by the model was at flow rate of 47.5 mL/min, MF loading of 50, and AC-Ag amount of 0.3 cm (**Table 5**). The numerical optimization function yielded a desirability value of 0.98 for this optimum point, indicating a near-ideal compromise between maximizing removal efficiency and the specified operational constraints. Validation experiments conducted under these conditions resulted in actual removal efficiencies of 94.66%, 95.33%, and 96.00%, averaging close to the model's predicted value of 98.12%, with a relative standard error (RSE) of less than 3.53%. The predicted vs. actual plot (**Figure 12**) shows excellent correlation, supporting the model's accuracy in forecasting system behaviour within the experimental range.

a)

b)

c)

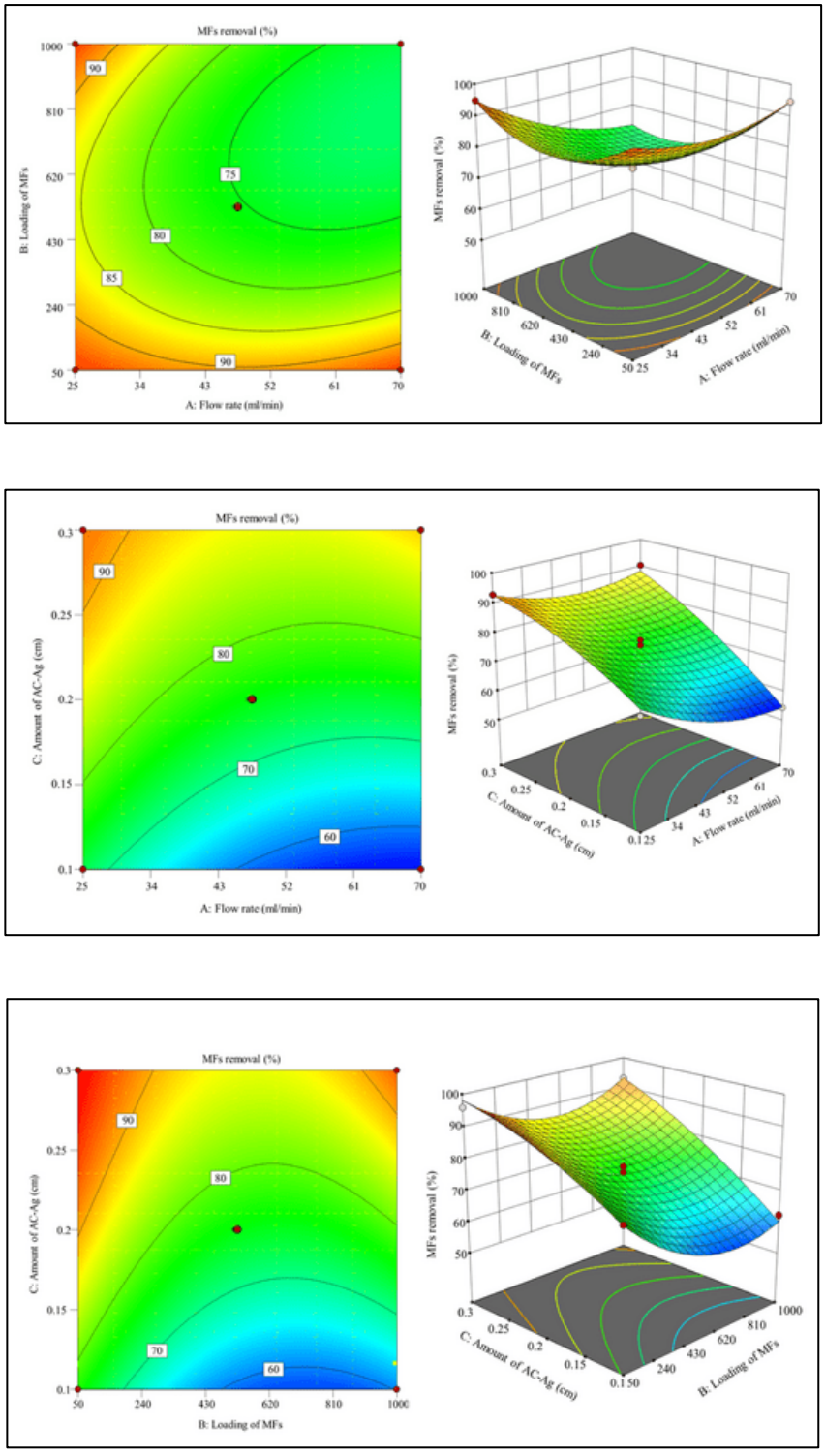

Figure 10. Effects of the variables of MFs removal (a) flow rate vs. loading of MFs, (b) flow rate vs. amount of AC-Ag, and (c) loading of MFs vs. amount of AC-Ag

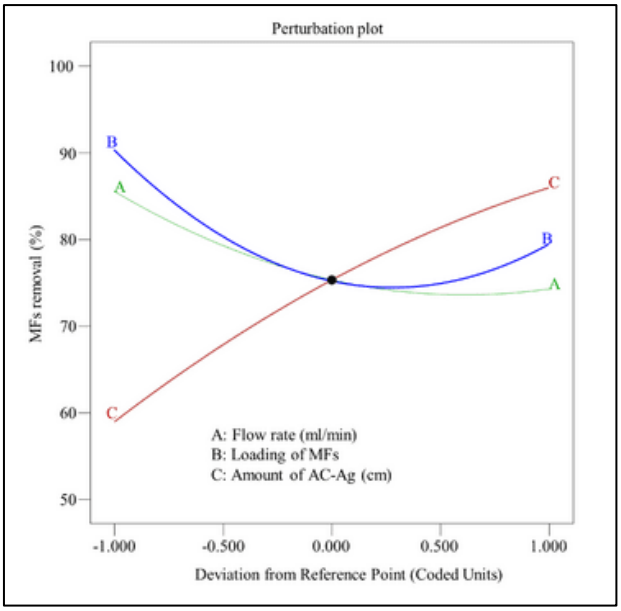

Figure 11. Perturbation plots of removal performance for MFs

Table 5. Predicted and experimental value under the optimum condition for removal efficiency of MFs

Run	Flow Rate (mL/min)	Loading of MFs	Amount of AC-Ag (cm)	Removal of MFs		Residual Standard Error (RSE, %)
				Actual	Predicted	
1	47.5	50	0.3	94.66	98.12	-3.53
2	47.5	50	0.3	95.33	98.12	-2.84
3	47.5	50	0.3	96.00	98.12	-2.16

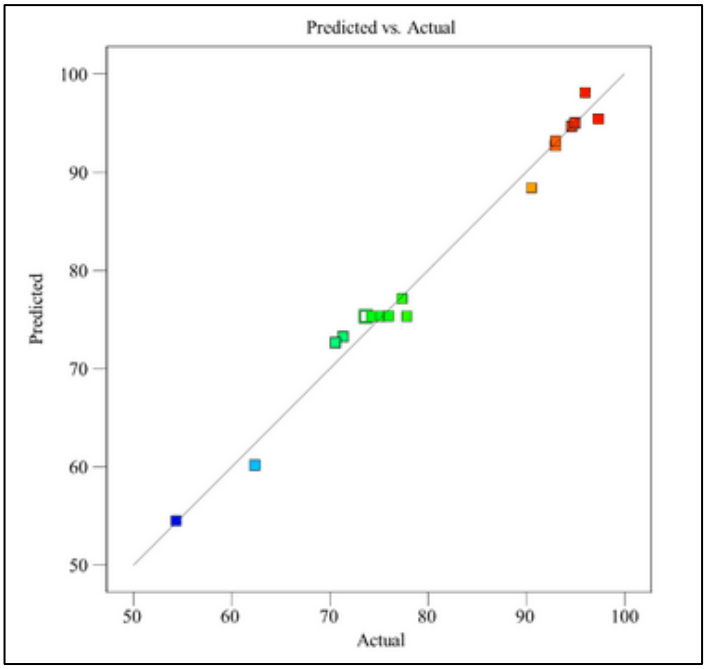

Figure 12. Predicted versus actual graph plot for the corresponding responses for removal performance of MFs

Conclusion

In summary, the integration of silver nanoparticles into rice husk-derived activated carbon produced a hybrid adsorbent (AC-Ag) with enhanced structural and functional properties suitable for MF removal. The porous carbon matrix, reinforced with crystalline Ag nanoparticles, provided both physical entrapment sites and improved surface interactions, allowing efficient capture of fibrous microplastics in fixed-bed column filtration. Filtration experiments revealed that AC-Ag significantly outperformed bare RHAC in removing MFs from domestic laundry effluents, achieving removal efficiencies up to 99%. The application of RSM-BBD effectively identified key operational parameters, highlighting adsorbent bed height and flow rate as dominant factors influencing removal efficiency. Optimal conditions yielded high model predictability ($R^2 = 0.9685$) and demonstrated that lower flow rates and thicker AC-Ag beds maximize MF retention through extended residence time and multilevel pore trapping. This work establishes AC-Ag derived from agricultural waste as a low-cost, sustainable, and highly effective adsorbent for mitigating MF pollution in laundry wastewater. Its performance and scalability indicate strong potential for integration into domestic and industrial wastewater treatment systems, contributing to microplastic pollution reduction and advancing circular waste utilization strategies.

Acknowledgement

The authors gratefully acknowledge financial support from the National Water Research Institute of Malaysia (NAHRIM) and Ministry of Environment and Water (Vot No. 53348), as well as Universiti Malaysia Terengganu for the research facilities provided.

References

1. Salahuddin, M., and Lee, Y.-A. (2022). Are laundry balls a sustainable washing option for consumers? Investigating the effect of laundry balls on microfiber pollution through the lens of cradle-to-cradle design model. *Sustainability, 14*(21), 14314.
2. Athey, S. N., and Erdle, L. M. (2022). Are we underestimating anthropogenic microfiber pollution? A critical review of occurrence, methods, and reporting. *Environmental Toxicology and Chemistry, 41*(4), 822–837.
3. Buss, N., Sander, B., and Hua, J. (2022). Effects of polyester microplastic fiber contamination on amphibian–trematode interactions. *Environmental Toxicology and Chemistry, 41*(4), 869–879.
4. Gavigan, J., Kefela, T., Macadam-Somer, I., Suh, S., and Geyer, R. (2020). Synthetic microfiber emissions to land rival those to waterbodies and are growing. *PLOS ONE, 15*(9), e0237839.
5. Cui, J., Yang, Y., Hu, Y., and Li, F. (2015). Rice husk-based porous carbon loaded with silver nanoparticles by a simple and cost-effective approach and their antibacterial activity. *Journal of Colloid and Interface Science, 455*, 117–124.
6. Devi, T. B., Mohanta, D., and Ahmaruzzaman, M. (2019). Biomass-derived activated carbon loaded silver nanoparticles: An effective nanocomposite for enhanced solar photocatalysis and antimicrobial activities. *Journal of Industrial and Engineering Chemistry, 76*, 160–172.
7. Gonçalves, S. P. C., Strauss, M., Delite, F. S., Clemente, Z., Castro, V. L., and Martinez, D. S. T. (2016). Activated carbon from pyrolysed sugarcane bagasse: Silver nanoparticle modification and ecotoxicity assessment. *Science of the Total Environment, 565*, 833–840.
8. Dawelbeit, A., and Yu, M. (2021). Tentative confinement of ionic liquids in nylon 6 fibers: A bridge between structural developments and high-performance properties. *ACS Omega, 6*(5), 3535–3547.
9. Rao, P. N., Sabavath, G., and Paul, S. (2021). Impact of MTA blend percentage in melt spinning process and polyester properties. *SN Applied Sciences, 3*(2), 184.
10. Gies, E. A., LeNoble, J. L., Noël, M., Etemadifar, A., Bishay, F., Hall, E. R., and Ross, P. S. (2018). Retention of microplastics in a major secondary wastewater treatment plant in Vancouver, Canada. *Marine Pollution Bulletin, 133*, 553–561.
11. Mintenig, S. M., Int-Veen, I., Löder, M. G. J., Primpke, S., and Gerdts, G. (2017). Identification of microplastic in effluents of wastewater treatment plants using focal plane array-based micro-Fourier-transform infrared imaging. *Water Research, 108*, 365–372.
12. Novotná, J., Tunák, M., Militký, J., Křemenáková, D., Wiener, J., Nováková, J., and Ševců, A. (2025). Release of microplastic fibers from polyester knit fleece during abrasion, washing, and drying. *ACS Omega, 10*(14), 14241–14249.
13. Periyasamy, A. P., and Tehrani-Bagha, A. (2022). A review on microplastic emission from textile materials and its reduction techniques. *Polymer Degradation and Stability, 199*, 109901.
14. Militký, J., Novotná, J., Wiener, J., Křemenáková, D., and Venkataraman, M. (2024). Microplastics and fibrous fragments generated during the production and maintenance of textiles. *Fibers, 12*(7), 51.
15. Yuliusman, Sipangkar, S. P., Fatkhurrahman, M., Farouq, F. A., and Putri, S. A. (2020). Utilization of coconut husk waste in the preparation of

activated carbon by using chemical activators of KOH and NaOH. *AIP Conference Proceedings, 2255*(1), 060026.

16. Yuliusman, Farouq, F. A., Sipangkar, S. P., Fatkhurrahman, M., and Putri, S. A. (2020). Preparation and characterization of activated carbon from corn stalks by chemical activation with KOH and NaOH. *AIP Conference Proceedings, 2255*(1), 060006.
17. Ramasundaram, S., Manikandan, V., Vijayalakshmi, P., Devanesan, S., Salah, M. B., Babu, A. R., Priyadharsan, A., Oh, T. H., and Ragupathy, S. (2023). Synthesis and investigation on synergetic effect of activated carbon loaded silver nanoparticles with enhanced photocatalytic and antibacterial activities. *Environmental Research, 233*, 116431.
18. Katta, V., Dubey, R., and Joshi, G. (2023). Experimental investigation of activated carbon nanoflakes produced by thermal and chemical activation processes. *Fullerenes, Nanotubes and Carbon Nanostructures, 31*(1), 10–17.
19. Soffian, M., Abdul Halim, F., Aziz, F., Rahman, A., Mohamed Amin, M., and Awang Chee, D. (2022). Carbon-based material derived from biomass waste for wastewater treatment. *Environmental Advances, 9*, 100259.
20. Meng, Y. (2015). A sustainable approach to fabricating Ag nanoparticles/PVA hybrid nanofiber and its catalytic activity. *Nanomaterials, 5*, 1124–1135.
21. Farooqi, M. A., Bae, S., Kim, S., Kausar, F., Farooqi, H. M. U., Hyun, C. G., and Kang, C. U. (2024). Eco-friendly synthesis of bioactive silver nanoparticles from black roasted gram (*Cicer arietinum*) for biomedical applications. *Scientific Reports, 14*(1), 22922.
22. Dao, M. U., Hoang, H. Y., Tran, A. K., and Cong, H. H. (2021). Assessment and treatment of floodwater in the Vietnamese Mekong Delta using a simple filter system based on silver nanoparticles coated onto activated carbon derived from rice husk. *RSC Advances, 11*(63), 39838–39847.
23. Zhao, Y., You, J., Wang, L., Bao, W., and Yao, R. (2021). Recent advances in Ni_3S_2-based electrocatalysts for oxygen evolution reaction. *International Journal of Hydrogen Energy, 46*(79), 39146–39182.
24. Sarkar, S., and Basak, D. (2013). One-step nano-engineering of dispersed Ag–ZnO nanoparticles hybrid in reduced graphene oxide matrix and its superior photocatalytic property. *CrystEngComm, 15*(37), 7606–7614.
25. Doğan, M., Sabaz, P., Biçil, Z., Kızılduman, B. K., and Turhan, Y. (2020). Activated carbon synthesis from tangerine peel and its use in hydrogen storage. *Journal of the Energy Institute, 93*(6), 2176–2185.
26. Chen, C., Qu, B., Wang, W., Ji, G., and Li, A. (2021). Rice husk and rice straw torrefaction: Properties and pyrolysis kinetics of raw and torrefied biomass. *Environmental Technology and Innovation, 24*, 101872.
27. Rahmat, A., Nissa, R., Nuraini, L., Nurtanto, M., and Ramadhani, W. (2023). Analysis of rice husk biochar characteristics under different pyrolysis temperature. *IOP Conference Series: Earth and Environmental Science*.
28. Faisal, H. A., Mohammed, A. K., Sbani, N. H. A., and Isaha, W. N. R. W. (2025). Comparative study of activated carbon and silver nanoparticle-loaded activated carbon derived from tea waste for removal of tetracycline from aqueous solution. *Tikrit Journal of Engineering Sciences, 32*(2), 1–17.
29. Wazir, A. H., Wazir, I. U., and Wazir, A. M. (2024). Preparation and characterization of rice husk-based physical activated carbon. *Energy Sources, Part A: Recovery, Utilization, and Environmental Effects, 46*(1), 4875–4885.
30. Serafin, J., and Dziejarski, B. (2024). Activated carbons—Preparation, characterization and their application in CO_2 capture: A review. *Environmental Science and Pollution Research, 31*(28), 40008–40062.
31. Pérez-Mayoral, E., Matos, I., Bernardo, M., and Fonseca, I. M. (2019). New and advanced porous carbon materials in fine chemical synthesis: Emerging precursors of porous carbons. *Catalysts, 9*(2), 133.
32. Li, P., Liu, J., and Zhang, H. (2022). Insights into the interaction of microplastic with silver nanoparticles in natural surface water. *Science of the Total Environment, 805*, 150315.
33. Wang, Z., Sedighi, M., and Lea-Langton, A. (2020). Filtration of microplastic spheres by biochar: Removal efficiency and immobilisation mechanisms. *Water Research, 184*, 116165.
34. Jaber, L., Backer, S. N., Laoui, T., Abumadi, F., Koujan, M. M. S., Khalil, K. A., Shanableh, A., and Atieh, M. A. (2024). Recent trends in surface impregnation techniques on activated carbon for efficient pollutant removal from wastewater. *Desalination and Water Treatment*, 100562.
35. Tavakoli, H., Hashemi, S., Amirkhani, R., and Gholampour, M. (2023). Silver nanoparticles loaded on silica nanoparticles and activated carbon prepared for use in portable water treatment. *Journal of Synthetic Chemistry, 1*(3), 137–147.
36. Acarer, S. (2023). A review of microplastic removal from water and wastewater by membrane technologies. *Water Science and Technology, 88*(1), 199–219.

37. Uogintė, I., Pleskytė, S., Pauraitė, J., and Lujanienė, G. (2022). Seasonal variation and complex analysis of microplastic distribution in different WWTP treatment stages in Lithuania. *Environmental Monitoring and Assessment, 194*(11), 829.
38. Rushdi, I. W., Hardian, R., Rusidi, R. S., Khairul, W. M., Hamzah, S., Khalik, W. M. A. W. M., Abdullah, N. S., Yahaya, N. K. E., Szekely, G., and Azmi, A. A. (2025). Microplastic and organic pollutant removal using imine-functionalized mesoporous magnetic silica nanoparticles enhanced by machine learning. *Chemical Engineering Journal, 510*, 161595.
39. Arenas, L. R., Gentile, S. R., Zimmermann, S., and Stoll, S. (2021). Nanoplastics adsorption and removal efficiency by granular activated carbon used in drinking water treatment process. *Science of the Total Environment, 791*, 148175.
40. Metcalf and Eddy, Abu-Orf, M., Bowden, G., Burton, F. L., Pfrang, W., Stensel, H. D., Tchobanoglous, G., Tsuchihashi, R., and AECOM. (2014). *Wastewater engineering: Treatment and resource recovery*. McGraw-Hill Education.
41. Subair, A., Krishnamoorthy Lakshmi, P., Chellappan, S., and Chinghakham, C. (2024). Removal of polystyrene microplastics using biochar-based continuous flow fixed-bed column. *Environmental Science and Pollution Research, 31*(9), 13753–13765.